Graphene nano-electromechanical mass sensor with high resolution at room temperature

Shin, Dong Hoon; Kim, Hakseong; Kim, Sung Hyun; Cheong, Hyeonsik; Steeneken, Peter G.; Joo, Chirlmin; Lee, Sang Wook

DOI
10.1016/j.isci.2023.105958

Publication date
2023

Document Version
Final published version

Published in
iScience

Citation (APA)
Shin, D. H., Kim, H., Kim, S. H., Cheong, H., Steeneken, P. G., Joo, C., & Lee, S. W. (2023). Graphene nano-electromechanical mass sensor with high resolution at room temperature. *iScience*, *26*(2), Article 105958. https://doi.org/10.1016/j.isci.2023.105958

iScience

CellPress
OPEN ACCESS

Article

Graphene nano-electromechanical mass sensor with high resolution at room temperature

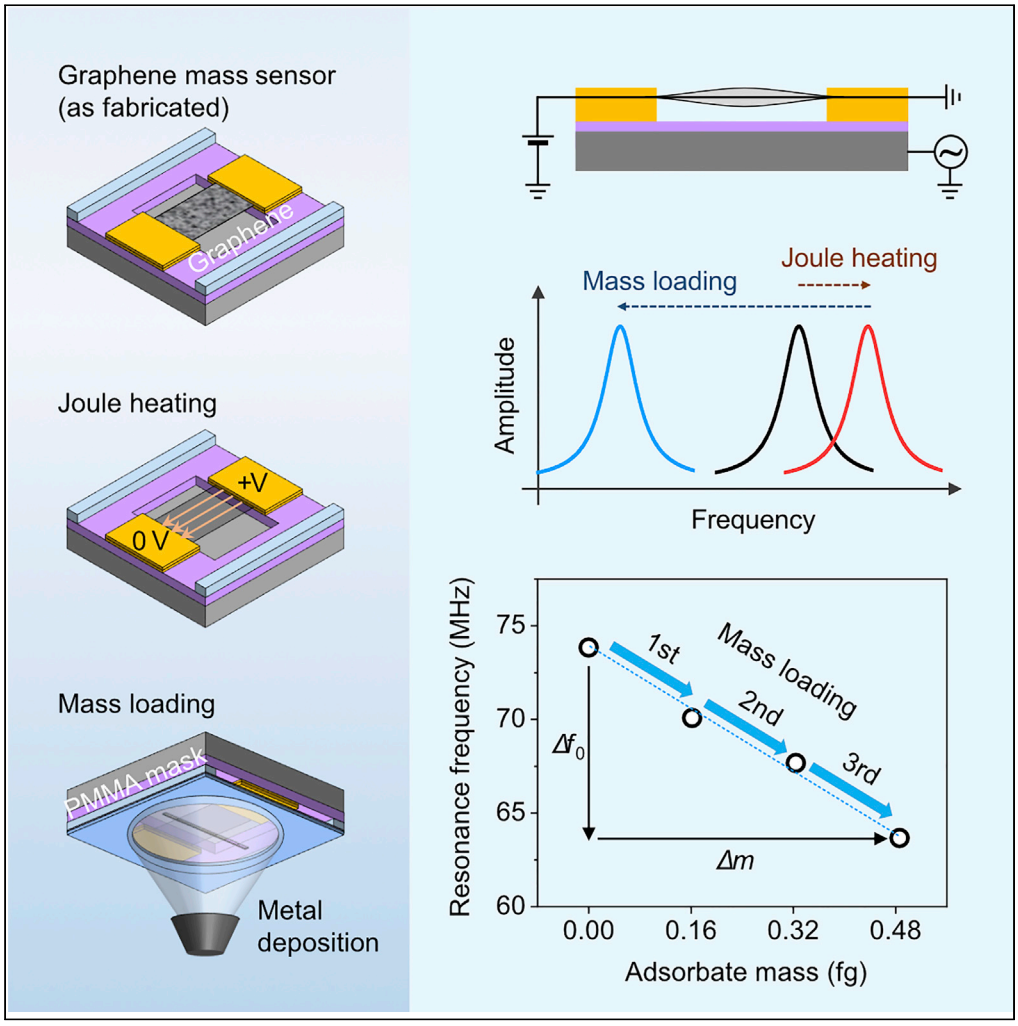

Dong Hoon Shin, Hakseong Kim, Sung Hyun Kim, Hyeonsik Cheong, Peter G. Steeneken, Chirlmin Joo, Sang Wook Lee

leesw@ewha.ac.kr

Highlights

A nanomechanical graphene mass sensor (GMS) is demonstrated

Joule heating improves the resonance frequency, frequency stability and Q factor

Sub-attogram mass resolution is achieved at room temperature

Potential applications of GMS in the nanobiology and medicine fields are proposed

Shin et al., iScience 26, 105958
February 17, 2023
https://doi.org/10.1016/j.isci.2023.105958

iScience

CellPress
OPEN ACCESS

Article

Graphene nano-electromechanical mass sensor with high resolution at room temperature

Dong Hoon Shin,[1,2,3,7] Hakseong Kim,[4,7] Sung Hyun Kim,[2,6] Hyeonsik Cheong,[5] Peter G. Steeneken,[2,3] Chirlmin Joo,[1,2,6] and Sang Wook Lee[1,8,*]

SUMMARY

The inherent properties of 2D materials—light mass, high out-of-plane flexibility, and large surface area—promise great potential for precise and accurate nano-mechanical mass sensing, but their application is often hampered by surface contamination. Here we demonstrate a tri-layer graphene nanomechanical resonant mass sensor with sub-attogram resolution at room temperature, fabricated by a bottom-up process. We found that Joule-heating is effective in cleaning the graphene membrane surface, which results in a large improvement in the stability of the resonance frequency. We characterized the sensor by depositing Cr metal using a stencil mask and found a mass-resolution that is sufficient to weigh very small particles, like large proteins and protein complexes, with potential applications in the fields of nanobiology and medicine.

INTRODUCTION

Mass is a fundamental property of matter, and mass spectrometry (MS) is one of the most effective analysis techniques, which has been used to identify different types of biomolecules such as deoxyribonucleic acids (DNA), ribonucleic acids (RNA), proteins, carbohydrates, and metabolites.[1–6] MS-based proteomics has advanced to the point where it allows for single-cell proteomics and intact analysis of biomolecules.[4,7–9] Recently, mass sensing based on nano-electromechanical systems (NEMS) has received much attention as a complementary technique to determine the molecular mass.[10–17] In contrast to current MS systems that use the mass-to-charge ratio to identify distributions of biomolecules, NEMS mass sensors hold the promise to directly determine mass of a single biomolecule from the resonance frequency shift of a suspended membrane. Among the various NEMS materials, 2D materials have recently been receiving much attention because of the following fundamental advantages. First, 2D materials have very small mass per area because of their atomic thicknesses, thus promising high mass resolution. Second, they are exceedingly flexible in the out-of-plane direction because of their small thicknesses, but yet greatly stiff in-plane because of their large Young's moduli; therefore, superior responsivity on the mechanical stimulus is expected.[18–21] Finally, their large surface area compared to other nanomaterials like carbon nanotubes increases the mass capture efficiency.

However, their low mass makes 2D material membranes extremely vulnerable to frequency variations, especially at room temperature. For example, surface contaminants and perpetual absorption/desorption of gases and liquids by these contaminants, which originate from the fabrication process, can lead to large frequency variations. Several methods have been suggested for achieving a contaminant-free surface of 2D materials; for instance, thermal annealing,[22–24] mechanical cleaning,[25–27] and UV ozone cleaning.[28,29] However, these non-local cleaning methods are often not applicable to mechanical resonator devices as they damage the suspended membrane or other device components.[28,30]

We here demonstrate Joule heating as an effective surface cleaning method for 2D NEMS mass sensors. Previously, annealing graphene by Joule heating has been proposed and demonstrated as an effective way to clean the graphene surface.[31,32] As it was later found that suspended graphene can be heated up to 2800 K by Joule heating while graphene maintains its structural robustness at such high temperatures,[33] it is expected that most of the organic and inorganic impurities left behind the manufacturing process can be effectively removed from graphene surface. When a current is run through a suspended 2D membrane, the Joule heating power is concentrated in the region with the highest sheet resistance. Because the temperature rise is highest in the region with highest thermal resistance to the heat sink, it allows annealing of the suspended part of the 2D

[1]Department of Physics, Ewha Womans University, Seoul 03760, Republic of Korea

[2]Kavli Institute of Nanoscience Delft, Lorentzweg 1, 2628 CJ Delft, the Netherlands

[3]Department of Precision and Microsystems Engineering, Delft University of Technology, Mekelweg 2, 2628 CD Delft, the Netherlands

[4]Korea Research Institute of Standards and Science (KRISS), Daejeon 34113, Republic of Korea

[5]Department of Physics, Sogang University, Seoul 04107, Republic of Korea

[6]Department of Bionanoscience, Delft University of Technology, 2629 HZ Delft, the Netherlands

[7]These authors contributed equally

[8]Lead contact

*Correspondence: leesw@ewha.ac.kr

https://doi.org/10.1016/j.isci.2023.105958

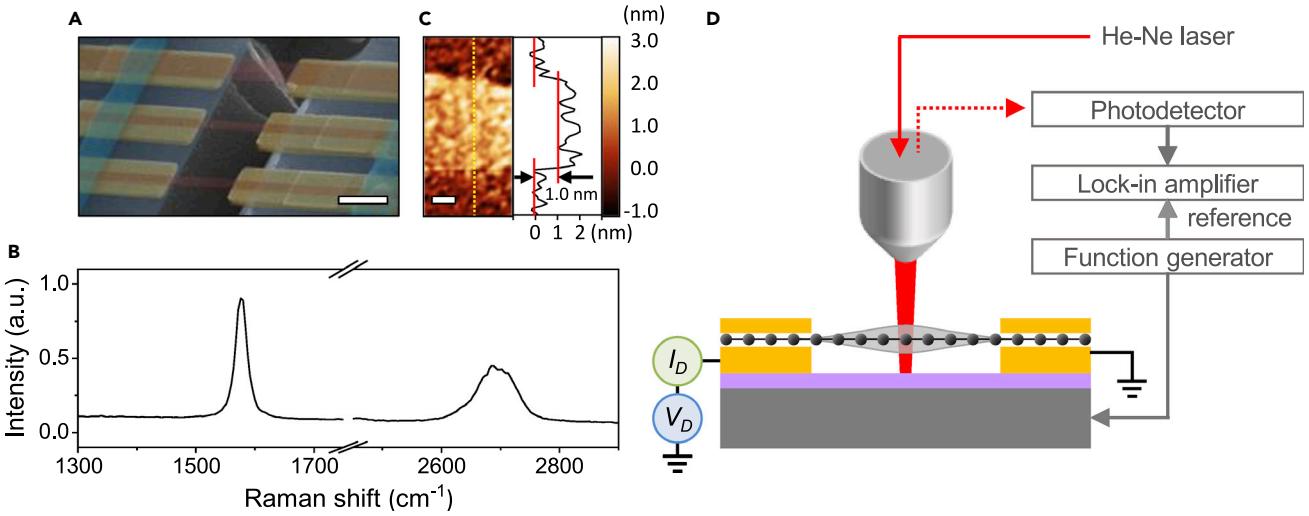

Figure 1. Characteristics of the graphene mass sensor and the setup for measuring the dynamic flexural motion of the suspended graphene membrane

(A) Scanning electron microscope image of the graphene mass sensor. The graphene used in this work (middle one) was electrically connected with gold electrodes in the both ends and had the dimension of 2.7 μm (*L*) and 0.75 μm (*w*) for the suspended part. The scale bar is 2 μm.

(B) D, G, and 2D peaks in Raman spectrum indicates that the graphene consists of three layers with a high crystallinity.

(C) Atomic force microscope image of the graphene transferred on the gold electrodes. The thickness of the graphene determined from the height profile measured along the yellow dashed line in the image was ~1.0 nm, corresponding to three atomic layers. The scale bar is 200 nm.

(D) Schematic illustration of the measurement setup. The graphene was actuated by electrostatic force between the graphene and the bottom gate. The heavily doped silicon substrate is used as a gate electrode, and dynamic flexural motion was measured using optical interferometry with a He-Ne laser, photodetector, and lock-in amplifier.

membrane that is most relevant for mass sensing. The metal electrodes function both as electric current supply and as heat sinks which prevent damage caused by overheating of the 2D membrane. In this study, we evaluate the mass sensing performance of graphene mass sensors at room temperature under low vacuum conditions by measuring the change in resonance frequency because of controlled deposition of chromium (Cr). After ultra-high temperature (UHT) annealing induced by Joule heating, the graphene mass sensor shows a stabilized resonance frequency and a sub-attogram level mass resolution.

RESULTS

Device fabrication and measurement setup

Graphene mass sensor devices were fabricated using electron beam lithography and graphene transfer techniques as described in the Method Details section and the Supplemental Information Section 1. Using scanning electron microscopy, we confirmed that the ribbon-shaped graphene membrane was well suspended over the trench without any signs of structural deformation or sagging as shown in Figure 1A. The suspended length and width of the graphene ribbon used in this study were determined to be 2.7 μm and 0.75 μm, respectively. The 2D peak shape, the 2D to G peak ratio, and the D peak intensity of the Raman spectrum in Figure 1B showed that the few-layer graphene membrane had three atomic layers and a high crystallinity.[34–36] This was also confirmed by atomic force microscopy of the graphene ribbon after it was transferred on the Au electrode (Figure 1C). Despite the rough surface of Au electrode and remaining residues, the height profile revealed that the thickness of the graphene ribbon was ~1.0 nm, which is equivalent to the three atomic layers. The dynamic flexural motion of the graphene mass sensor was measured using optical interferometry, with a He-Ne laser, photodetector and lock-in amplifier, as illustrated in Figure 1D.[21,37,38] The suspended graphene membrane was actuated by an electrostatic force that was applied between the graphene and the bottom gate electrode. The resonance frequency and quality (*Q*) factor of the graphene ribbon resonator were obtained by fitting a Lorentzian curve to the frequency response plot (See Figure S3 and Table S1).

Ultra-high temperature annealing by Joule heating

To carefully anneal the graphene mass sensor at an ultra-high temperature by Joule heating, we performed successive drain voltage (V_D) sweeps, while gradually increasing the maximally applied voltage V_D, as

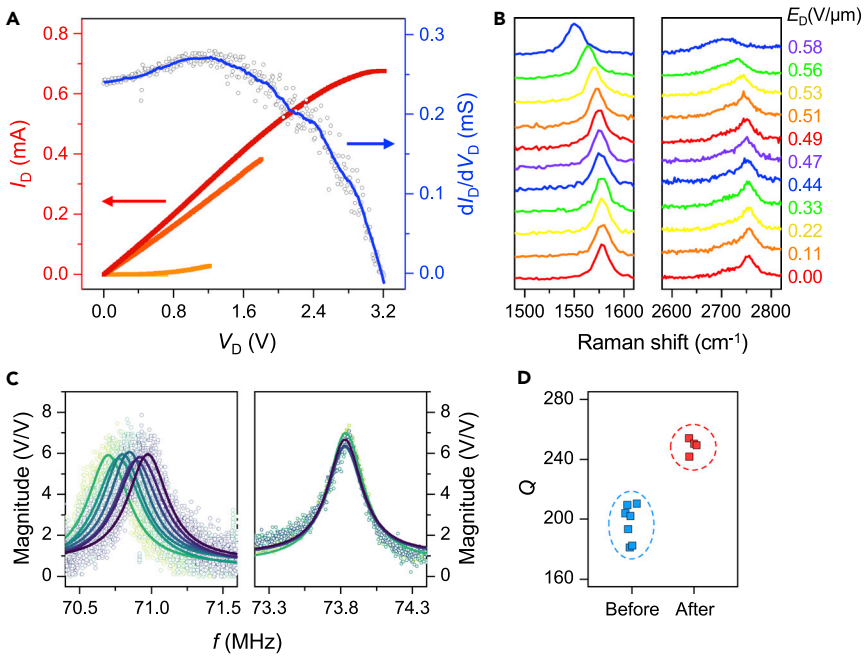

Figure 2. Joule-heating effects on the graphene mass sensor

(A) I_D (red and orange) and dI_D/dV_D (blue) measurements of the graphene mass sensor are shown as a function of V_D. Three subsequent I_D-V_D curves are shown, the first (orange) up to 1.2 V, the second (dark orange) up to V_D = 1.7 V, and the last (red) up to 3.2 V. The dI_D/dV_D of the red curve, which is smoothed by the Savitzky-Golay filter, is shown in blue.

(B) Raman spectra measured from a suspended three layer (3L) graphene sample with a length and a width of 9 μm and 3 μm, respectively, during the Joule heating process. The electric field strengths E_D are indicated by line colors and values besides the graph. Red shifts in the G and 2D peaks are clearly seen from 0.44 V/μm (V_D = 4.0 V).

(C) Measurement of the resonance frequencies of the graphene mass sensor before (left) and after (right) the Joule-heating. The scattered dots represent data points obtained from the frequency sweep measurements. A Lorentzian fit to the data (solid lines) gives the resonance frequency and Q factor of each frequency sweep dataset. The resonance frequency of the pristine graphene mass sensor shifts during the measurements whereas that of the device becomes stabilized significantly after the Joule heating process.

(D) Q factors obtained by fitting the frequency sweep data measured before and after the Joule-heating process with Lorentzian curves.

shown in Figure S2 performed with a different device. The annealing process was conducted in a high vacuum chamber. When we applied voltages V_D of less than 1.2 V, the I_D-V_D curve was non-linear, while showing a very high resistance of a few MΩ as shown in Figure 2A, which we attribute to a high initial contact resistance between the graphene ribbon and the metal electrodes after the transfer process. However, after several voltage sweeps, the resistance dramatically decreased to 3.9 kΩ, indicative of the formation of a good contact (Figure 2A, red and orange lines). When we increased V_D up to 3.2 V, the I_D-V_D characteristics exhibited a current saturation behavior and a reduced differential conductance (Figure 2A, blue scattered dots and line). At the same time, light emission in the visible range was observed from the suspended graphene. Both the initiation of the visible light and zero differential conductance suggest that the graphene temperature became higher than 2000 K.[33] Despite the ultra-high temperature exceeding 2000 K, the Joule heating was not observed to result in damage to the device or its surroundings, which we attribute to the confinement of heat to the suspended part of the membrane and to cooling by metal electrodes that act as heat sinks.[33]

Figure 2B shows the Raman spectra measured from another suspended three layer (3L) graphene sample with a length and a width of 9 μm and 3 μm, respectively, during the Joule heating process. The device started emitting visible light at an electric field (E_D) of 0.44 V/μm between source and drain electrodes and became brighter as E_D increased. At the same time, a significant shift in G and 2D peak positions was observed, implying a change in the atomic structure. Owing to its negative thermal expansion coefficient, the atomic structure of graphene is expected to be compressed at high temperature, causing a

tensile stress across the suspended graphene when both ends are fixed.[33,39–41] This effect was observed in the Raman data, in which G and 2D peak positions shifted from 1580 to 1540 cm^{-1} and from 2750 to 2700 cm^{-1}, respectively, as E_D increased from 0 to 0.58 V/μm. Taking into account both thermal and strain effects,[41] the strain calculated from the shift of the G peak is in the range of 0.3–1.0% at E_D = 0.58 V/μm,[42,43] which indicates that the structural deformation because of Joule heating was still in the elastic regime, as it is known that plastic deformation or structural rupture occurs above ~13–19% (theoretical results) and ~1.2–6% (experimental results).[19,44–47]

Figure 2C represents the fundamental mode resonance of the graphene mass sensor before (left) and after (right) annealing. Frequency sweeps were performed with an integration time of 0.1 s, and then the resonance frequencies (f_0) and Q factors were extracted through Lorentzian fitting of a magnitude-frequency curve. The mean resonance frequency ($\overline{f_0}$) of the graphene ribbon resonator increased from 70.84 to 73.83 MHz after the UHT annealing. If we assume this frequency shift is due to the mass removed from the graphene surface by annealing, the mass reduction can be estimated to be $\delta m = -\frac{2M_{eff}}{f_0[\varphi(x)]^2}\Delta f$, where δm, M_{eff}, f_0, Δf, $\varphi(x)$ represent respectively the mass change, effective mass of the resonator, resonance frequency, resonance frequency change, and fundamental resonance mode shape at the normalized adsorbate position with the normalization condition $max(\varphi(x)) = 1$, which considers the influence of the adsorbate position on the resonance frequency shift.[11,12,48–50] The M_{eff} of a doubly clamped graphene resonator for the fundamental mode is given by $lw\rho \int_{x=0}^{x=1} [\varphi(x)]^2 dx = 0.5\, lw\rho$, where l, w, and ρ are length, width, and areal mass density of the graphene resonator, respectively.[51] By assuming the graphene areal mass density of tri-layer graphene, $\rho_{3L} = 2.28 \times 10^{-6}$ kg/m^2 ($\rho_{1L} = 7.6 \times 10^{-7}$ kg/m^2),[52] and ignoring the stiffness effect by adsorption, the total mass eliminated from the graphene surface is estimated to be 0.37 fg, which might be attributed to polymer residues that were on the suspended graphene after the transfer procedure. The actual mass can be slightly larger than this estimate because the adsorption-induced stiffness effect is not taken into account here.[50,53]

The UHT annealing not only increases the resonance frequency but also considerably improves the frequency stability and the Q factor of the graphene mass sensor, as clearly seen by the resonance frequency changes over time in Figure S4 and the comparison plot in Figure 2D, respectively. A drift in resonance frequency (0.27 MHz for about 10 min) observed from the pristine graphene mass sensor decreased to a negligible level after high temperature annealing (Figure S4). The enhancement of the resonance frequency stability after cleaning graphene by UHT annealing shows that contaminants can play a significant role in the instability of the resonance frequency, which was also suggested by others by demonstrating that the resonance frequency fluctuation of a carbon nanotube resonator is substantially reduced after Joule heating.[48] Although more study will be needed to pinpoint the microscopic role of contaminants on the frequency stability, adsorption-desorption kinetics as well as diffusion of adsorbed molecules might contribute to the resonance frequency instability of our device, among many different sources of frequency instability.[54–58] When a material with high surface energy such as organic contaminants is attached to the graphene surface, a more active adsorption/desorption process may occur, and this process may be further accelerated by laser-induced heat.

Mass sensing performance

After the UHT annealing, we investigated the device performance of the graphene mass sensor by measuring resonance frequency changes while loading mass onto the suspended graphene. Instead of loading mass on the entire chip, we deposited Cr by electron beam evaporation on a selective device area by using a Poly(methyl methacrylate) (PMMA) stencil mask[59] with a slit of 0.5 μm × 50 μm (Figure 3A). The PMMA stencil mask not only minimized the amount of the mass, but also protected both ends of the suspended graphene from the metal evaporation process. The line slit pattern on the PMMA stencil mask was aligned to the center position of the suspended graphene ribbon. The graphene area of 0.75 μm (graphene width) by 0.5 μm (mask slit width) was exposed to 2 Å of Cr. The deposition thickness was measured using a quartz crystal microbalance. Considering the thickness of the PMMA stencil mask (~550 nm), the slit width (500 nm), and the divergence of the evaporated atomic beam, the relative deposition rate was about 0.3 because of masking effects,[60] which implies that a mass of 0.16 fg was loaded on the graphene surface for each step of Cr evaporation.

The resonance frequency was characterized after every deposition step, showing that the resonance frequency shifted downward after Cr deposition as expected (Figure 3B). From the linear fit of the resonance frequency shift versus mass shown in Figure 3C (blue dotted line), the mass responsivity $|\delta m/\delta f|$ of our graphene resonator was determined to be 47.8 ± 2.2 yg/Hz, which is close to but slightly different from the

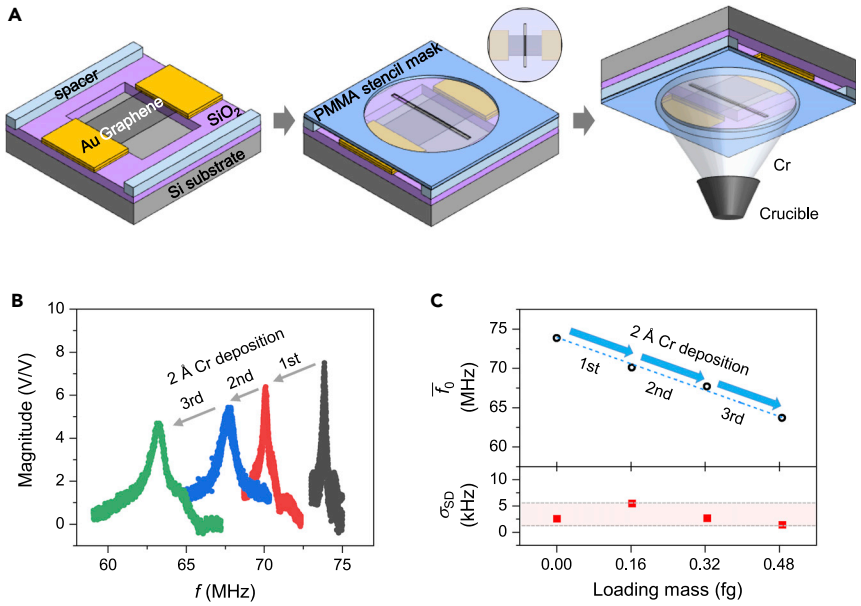

Figure 3. Measurements of resonance frequency changes while loading mass onto the suspended graphene

(A) Experimental procedures to load mass (Cr) onto graphene mass sensor. Cr was deposited onto the middle of the suspended graphene membrane through the PMMA shadow mask slit. The deposition thickness was monitored by a quartz crystal microbalance near the device to deposit 2 Å of Cr for each run.

(B) Resonance frequency change after the each run of the mass loading. The resonance frequencies were 73.8, 70.1, 67.7, and 63.7 MHz after each deposition step, respectively.

(C) Mean resonance frequency (upper panel) and SD(lower panel) changes as a function of mass loaded on the graphene mass sensor after annealing.

theoretical value of 62.5 yg/Hz calculated by $2M_{eff}/f_0$. The discrepancy between the two mass responsivities probably stems from the uncertainty in the amount of the actual mass loading.

When a mechanical resonator has an adsorbate layer of relatively substantial thickness covering the entire area of the resonator, the resonance frequency can be affected by the stiffness of the adsorbates. The adsorbate stiffness effect is positively dependent on the contact area between the adsorbate and the resonator, as well as the size and the elastic modulus of the adsorbate.[50] However, in the case of our mass loading experiments, the elastic modulus of graphene, ~1 TPa,[18–20] is much higher than that of adsorbed Cr nanoparticles, which is much smaller than 43 GPa, considering the size effect.[61,62] Furthermore, the deposition thickness (2 Å) is smaller than the diameter of Cr atoms (2.8–3.3 Å), and both the size of the deposited Cr and the contact area between the adsorbate and the resonator are extremely small. As a result, the adsorption-induced stiffness effect was neglected in estimating the load mass.

The minimum detectable mass (δm_{min}) of the resonant sensor can be determined to be $\delta m_{min}=(2M_{eff}/f_0) \times \delta f$, where δf is the frequency fluctuation of the resonator, in order for the mass induced frequency shift to exceed the frequency fluctuations.[63] By using the standard deviation(σ_{SD}) of the resonance frequencies across several measurements as the frequency fluctuations of the graphene mass sensor (Figure S5 and Table S1), the actual δm_{min} is calculated to be 0.16 ag (94 kDa) after the UHT annealing process. The σ_{SD} of the resonance frequencies is maintained below 5.5 kHz even after loading mass, as shown in Figure 3D, which corresponds to $\delta m_{min} \approx 0.34$ ag (205 kDa). An estimation of the uncertainty in the σ_{SD} of frequency measurements can be obtained by calculating the standard error (SE_{SD}) of the σ_{SD}: $SE_{SD} = \sigma_{SD}\sqrt{1-\frac{2}{n-1}\left[\frac{\Gamma\left(\frac{n}{2}\right)}{\Gamma\left(\frac{n-1}{2}\right)}\right]^2}$, where $\Gamma(\ )$, n are the gamma function and the sample size (*i.e.* the number of repeated measurements), respectively.[64,65] For estimating the SE_{SD}, we assume that our measurement data points have a normal distribution and are uncorrelated. The maximum SE_{SD} of the σ_{SD} after the first mass deposition is estimated to be 2.14 kHz, providing the greatest σ_{SD} among our measurement data, leading to a maximum value of σ_{SD} and δm_{min} of 7.6 kHz and 0.47 ag (294 kDa), respectively.

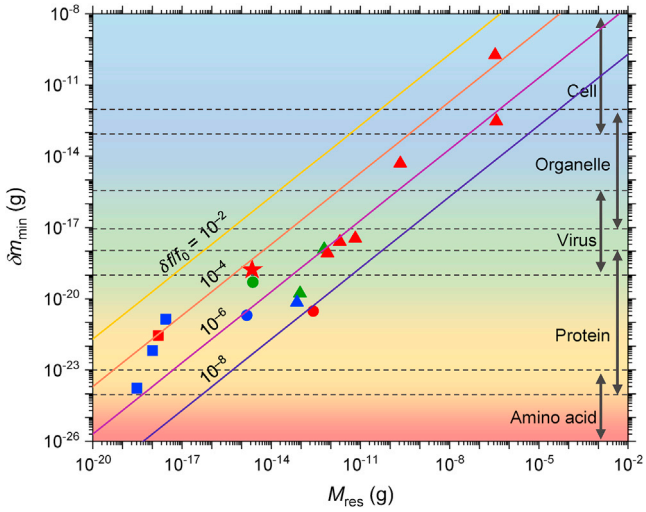

Figure 4. The minimum detectable mass (δm_{min}) and the mass of the NEMS resonant mass sensor (M_{res}) determined from literature (square, 1D material; circle, 2D material; triangle, 3D material) and our experiment data (star)

Color represents the temperature during the measurement (4 K < blue <6 K; 40 K < green <77 K; red, room temperature). The solid lines indicate the fractional frequency fluctuation ($\delta f/f_0$) determined as $\delta m_{min}/2M_{res}$. To simplify the comparison, M_{res} was considered to be equivalent to M_{eff}.

DISCUSSION

Figure 4 and Table S2 summarize the relation between the mass M_{res} of a resonator and its minimum detectable mass δm, as determined from literature data.[10,12,15–17,31,48,66–74] Most results have the fractional frequency fluctuation in the range of 10^{-4} –10^{-6}, with the solid trendlines in the figure indicating a mass resolution proportional to the resonator mass. The figure shows that identifying molecules in the mass range of MDa, which is a challenge in MS, can relatively easily performed with NEMS mass sensors, and furthermore, protein analysis and identification at single-molecule level is achievable if the resonator mass and the frequency fluctuation can be minimized sufficiently. However, when the resonator mass decreases, the fractional frequency fluctuation increases and the device area becomes too small to efficiently trap molecules, which poses potential challenges to obtaining high mass-resolution sensing. These challenges are especially big at room temperature, because the thermomechanical motion of the resonator is significantly larger at high temperature.

Ultrasensitive mass sensors utilizing the inherent advantages of 2D materials have been proposed by several research groups for several years.[18,75–79] However, there have been only a few cases of measuring actual mass using 2D NEMS mass sensors. Most of the papers reported values predicted by numerical calculation using the dynamic mechanical properties of the 2D resonators, not derived by actual mass measurements. To our best knowledge, there are only three cases in which mass was actually measured on a 2D resonator, which are shown in Figure 4.[31,70,73] Among these, two cases were carried out in extreme environments such as ultra-high vacuum and low temperature, which are far from the conditions for measuring biomolecules. In this study, we demonstrated the actual performance of the graphene mass sensor by loading mass and measuring the mass at room temperature.

We note that a promising biosensing platform where this NEMS device can be used is proteoform analysis. Although DNA contains the genetic information, which is translated into proteins, each known protein can have many different forms, called proteoform, which arise through RNA alternative splicing and post-translational modification (PTM). The use of traditional bottom-up mass spectrometry is complicated by protein fragmentation, which often eliminates the signature of splicing and PTMs.[5,80,81] NEMS mass sensing does not face this challenge and can be used for independently measuring the mass of single proteins without fragmentation, to obtain the mass distribution in the proteoform, especially in the large mass range. In cancer and other changes in physiology, the proteoforms can become aberrant with many new protein variants resulting from non-canonical splicing, mutations, fusions, and a wide range of PTMs. Detection of these

changes using NEMS will help determine the difference between health and disease, promising applications in both fundamental research and medical sciences. The potential of 2D materials as a mass sensor with a sub-attogram mass resolution in a readily accessible level of measurement environment, which is demonstrated in our study, paves a way for measuring large biological objects such as viruses and performing proteoform analysis.

LIMITATIONS OF THE STUDY

Further work needs to be done to measure the actual biomolecule mass. To avoid unwanted sample contamination that can occur between mass loading and measurement and to enable continuous measurements, specific equipment capable of measuring the resonant frequency change during mass deposition is required. The method utilized in this study to determine the resonance frequency and frequency stability is prone to systematic error. Because mass resolution is proportional to the standard deviation, the standard deviation calculated from a limited number of repeated frequency sweep measurements has relatively substantial uncertainty in estimating the mass resolution (0.21–0.47 ag).

STAR★METHODS

Detailed methods are provided in the online version of this paper and include the following:

- KEY RESOURCES TABLE
- RESOURCE AVAILABILITY
  - Lead contact
  - Materials availability
  - Data and code availability
- METHOD DETAILS
  - Fabrication of graphene resonators
  - Joule heating-induced ultra-high temperature annealing
  - Raman spectroscopy measurement
  - Dynamic flexural measurement
  - Preparation of PMMA stencil mask

SUPPLEMENTAL INFORMATION

Supplemental information can be found online at https://doi.org/10.1016/j.isci.2023.105958.

ACKNOWLEDGMENTS

S.W.L. and C.J. were supported by Human Frontier Science Program (RGP00026/2019). S.W.L was supported by the Basic Science Research Program (NRF-2022R1A2B5B01001640, NRF-2021R1A6A1A10039823) and Global Research and Development Center Program (NRF-2018K1A4A3A01064272) through the National Research Foundation of Korea (NRF). P.G.S. acknowledges funding from the European Union's Horizon 2020 research and innovation program under grant agreement number 881603 (Graphene Flagship). D.H.S acknowledges support from Basic Science Research Program (NRF-2017R1D1A1B03035727) through the National Research Foundation of Korea funded by the Ministry of Education and the KIND fellowship program at the Kavli Institute of Nanoscience Delft.

AUTHOR CONTRIBUTIONS

D.H.S., H.K., and S.W.L. conceived the study. H.K. and D.H.S. obtained and analyzed the data. D.H.S., H.K., S.H.K. H.C., C.J., P.G.S., and S.W.L. discussed the data and wrote the manuscript.

DECLARATION OF INTERESTS

The authors declare no competing interests.

Received: October 4, 2022
Revised: December 26, 2022
Accepted: January 8, 2023
Published: February 17, 2023

REFERENCES

1. Aebersold, R., and Mann, M. (2016). Mass-spectrometric exploration of proteome structure and function. Nature *537*, 347–355. https://doi.org/10.1038/nature19949.

2. Aksenov, A.A., da Silva, R., Knight, R., Lopes, N.P., and Dorrestein, P.C. (2017). Global chemical analysis of biology by mass spectrometry. Nat. Rev. Chem *1*, 0054. https://doi.org/10.1038/s41570-017-0054.

3. Bauermeister, A., Mannochio-Russo, H., Costa-Lotufo, L.V., Jarmusch, A.K., and Dorrestein, P.C. (2022). Mass spectrometry-based metabolomics in microbiome investigations. Nat. Rev. Microbiol. *20*, 143–160. https://doi.org/10.1038/s41579-021-00621-9.

4. Tamara, S., den Boer, M.A., and Heck, A.J.R. (2021). High-resolution native mass spectrometry. Chem. Rev. *122*, 7269–7326. https://doi.org/10.1021/acs.chemrev.1c00212.

5. Timp, W., and Timp, G. (2020). Beyond mass spectrometry, the next step in proteomics. Sci. Adv. *6*, eaax8978. https://doi.org/10.1126/sciadv.aax8978.

6. Wetzel, C., and Limbach, P.A. (2016). Mass spectrometry of modified RNAs: recent developments. Analyst *141*, 16–23. https://doi.org/10.1039/C5AN01797A.

7. Cui, W., Rohrs, H.W., and Gross, M.L. (2011). Top-down mass spectrometry: recent developments, applications and perspectives. Analyst *136*, 3854–3864. https://doi.org/10.1039/c1an15286f.

8. Schoof, E.M., Furtwängler, B., Üresin, N., Rapin, N., Savickas, S., Gentil, C., Lechman, E., Keller, U.A.d., Dick, J.E., and Porse, B.T. (2021). Quantitative single-cell proteomics as a tool to characterize cellular hierarchies. Nat. Commun. *12*, 3341. https://doi.org/10.1038/s41467-021-23667-y.

9. Specht, H., Emmott, E., Petelski, A.A., Huffman, R.G., Perlman, D.H., Serra, M., Kharchenko, P., Koller, A., and Slavov, N. (2021). Single-cell proteomic and transcriptomic analysis of macrophage heterogeneity using SCoPE2. Genome Biol. *22*, 50. https://doi.org/10.1186/s13059-021-02267-5.

10. Dominguez-Medina, S., Fostner, S., Defoort, M., Sansa, M., Stark, A.K., Halim, M.A., Vernhes, E., Gely, M., Jourdan, G., Alava, T., et al. (2018). Neutral mass spectrometry of virus capsids above 100 megadaltons with nanomechanical resonators. Science *362*, 918–922. https://doi.org/10.1126/science.aat6457.

11. Hanay, M.S., Kelber, S., Naik, A.K., Chi, D., Hentz, S., Bullard, E.C., Colinet, E., Duraffourg, L., and Roukes, M.L. (2012). Single-protein nanomechanical mass spectrometry in real time. Nat. Nanotechnol. *7*, 602–608. https://doi.org/10.1038/nnano.2012.119.

12. Naik, A.K., Hanay, M.S., Hiebert, W.K., Feng, X.L., and Roukes, M.L. (2009). Towards single-molecule nanomechanical mass spectrometry. Nat. Nanotechnol. *4*, 445–450. https://doi.org/10.1038/nnano.2009.152.

13. Sage, E., Brenac, A., Alava, T., Morel, R., Dupré, C., Hanay, M.S., Roukes, M.L., Duraffourg, L., Masselon, C., and Hentz, S. (2015). Neutral particle mass spectrometry with nanomechanical systems. Nat. Commun. *6*, 6482. https://doi.org/10.1038/ncomms7482.

14. Sage, E., Sansa, M., Fostner, S., Defoort, M., Gély, M., Naik, A.K., Morel, R., Duraffourg, L., Roukes, M.L., Alava, T., et al. (2018). Single-particle mass spectrometry with arrays of frequency-addressed nanomechanical resonators. Nat. Commun. *9*, 3283. https://doi.org/10.1038/s41467-018-05783-4.

15. Sansa, M., Defoort, M., Brenac, A., Hermouet, M., Banniard, L., Fafin, A., Gely, M., Masselon, C., Favero, I., Jourdan, G., and Hentz, S. (2020). Optomechanical mass spectrometry. Nat. Commun. *11*, 3781. https://doi.org/10.1038/s41467-020-17592-9.

16. Stassi, S., De Laurentis, G., Chakraborty, D., Bejtka, K., Chiodoni, A., Sader, J.E., and Ricciardi, C. (2019). Large-scale parallelization of nanomechanical mass spectrometry with weakly-coupled resonators. Nat. Commun. *10*, 3647. https://doi.org/10.1038/s41467-019-11647-2.

17. Yuksel, M., Orhan, E., Yanik, C., Ari, A.B., Demir, A., and Hanay, M.S. (2019). Nonlinear nanomechanical mass spectrometry at the single-nanoparticle level. Nano Lett. *19*, 3583–3589. https://doi.org/10.1021/acs.nanolett.9b00546.

18. Bunch, J.S., van der Zande, A.M., Verbridge, S.S., Frank, I.W., Tanenbaum, D.M., Parpia, J.M., Craighead, H.G., and McEuen, P.L. (2007). Electromechanical resonators from graphene sheets. Science *315*, 490–493. https://doi.org/10.1126/science.1136836.

19. Cao, K., Feng, S., Han, Y., Gao, L., Hue Ly, T., Xu, Z., and Lu, Y. (2020). Elastic straining of free-standing monolayer graphene. Nat. Commun. *11*, 284. https://doi.org/10.1038/s41467-019-14130-0.

20. Lee, C., Wei, X., Kysar, J.W., and Hone, J. (2008). Measurement of the elastic properties and intrinsic strength of monolayer graphene. Science *321*, 385–388. https://doi.org/10.1126/science.1157996.

21. Steeneken, P.G., Dolleman, R.J., Davidovikj, D., Alijani, F., and van der Zant, H.S.J. (2021). Dynamics of 2D material membranes. 2D Mater. *8*, 042001. https://doi.org/10.1088/2053-1583/ac152c.

22. Gong, C., Floresca, H.C., Hinojos, D., McDonnell, S., Qin, X., Hao, Y., Jandhyala, S., Mordi, G., Kim, J., Colombo, L., et al. (2013). Rapid selective etching of PMMA residues from transferred graphene by carbon dioxide. J. Phys. Chem. C *117*, 23000–23008. https://doi.org/10.1021/jp408429v.

23. Wang, X., Dolocan, A., Chou, H., Tao, L., Dick, A., Akinwande, D., and Willson, C.G. (2017). Direct observation of poly(methyl methacrylate) removal from a graphene surface. Chem. Mater. *29*, 2033–2039. https://doi.org/10.1021/acs.chemmater.6b03875.

24. Xie, W., Weng, L.-T., Ng, K.M., Chan, C.K., and Chan, C.-M. (2015). Clean graphene surface through high temperature annealing. Carbon *94*, 740–748. https://doi.org/10.1016/j.carbon.2015.07.046.

25. Jalilian, R., Jauregui, L.A., Lopez, G., Tian, J., Roecker, C., Yazdanpanah, M.M., Cohn, R.W., Jovanovic, I., and Chen, Y.P. (2011). Scanning gate microscopy on graphene: charge inhomogeneity and extrinsic doping. Nanotechnology *22*, 295705. https://doi.org/10.1088/0957-4484/22/29/295705.

26. Liu, Z., Bøggild, P., Yang, J.r., Cheng, Y., Grey, F., Liu, Y.l., Wang, L., and Zheng, Q.s. (2011). A graphite nanoeraser. Nanotechnology *22*, 265706. https://doi.org/10.1088/0957-4484/22/26/265706.

27. Sun, L., Lin, L., Wang, Z., Rui, D., Yu, Z., Zhang, J., Li, Y., Liu, X., Jia, K., Wang, K., et al. (2019). A force-engineered lint roller for superclean graphene. Adv. Mater. *31*, 1902978. https://doi.org/10.1002/adma.201902978.

28. Froning, J.P., Lazar, P., Pykal, M., Li, Q., Dong, M., Zbořil, R., and Otyepka, M. (2017). Direct mapping of chemical oxidation of individual graphene sheets through dynamic force measurements at the nanoscale. Nanoscale *9*, 119–127. https://doi.org/10.1039/C6NR05799C.

29. Mulyana, Y., Uenuma, M., Ishikawa, Y., and Uraoka, Y. (2014). Reversible oxidation of graphene through ultraviolet/ozone treatment and its nonthermal reduction through ultraviolet irradiation. J. Phys. Chem. C *118*, 27372–27381. https://doi.org/10.1021/jp508026g.

30. Liu, M., Shi, J., Li, Y., Zhou, X., Ma, D., Qi, Y., Zhang, Y., and Liu, Z. (2017). Temperature-triggered sulfur vacancy evolution in monolayer MoS_2/graphene heterostructures. Small *13*, 1602967. https://doi.org/10.1002/smll.201602967.

31. Chen, C., Rosenblatt, S., Bolotin, K.I., Kalb, W., Kim, P., Kymissis, I., Stormer, H.L., Heinz, T.F., and Hone, J. (2009). Performance of monolayer graphene nanomechanical resonators with electrical readout. Nat. Nanotechnol. *4*, 861–867. https://doi.org/10.1038/nnano.2009.267.

32. Moser, J., Barreiro, A., and Bachtold, A. (2007). Current-induced cleaning of graphene. Appl. Phys. Lett. *91*, 163513. https://doi.org/10.1063/1.2789673.

33. Kim, Y.D., Kim, H., Cho, Y., Ryoo, J.H., Park, C.-H., Kim, P., Kim, Y.S., Lee, S., Li, Y., Park, S.-N., et al. (2015). Bright visible light emission from graphene. Nat. Nanotechnol. *10*, 676–681. https://doi.org/10.1038/nnano.2015.118.

34. Malard, L.M., Pimenta, M.A., Dresselhaus, G., and Dresselhaus, M.S. (2009). Raman spectroscopy in graphene. Phys. Rep. *473*,

51–87. https://doi.org/10.1016/j.physrep.2009.02.003.

35. Nguyen, T.A., Lee, J.-U., Yoon, D., and Cheong, H. (2014). Excitation energy dependent Raman signatures of ABA- and ABC-stacked few-layer graphene. Sci. Rep. *4*, 4630. https://doi.org/10.1038/srep04630.

36. Yoon, D., Moon, H., Cheong, H., Choi, J., Choi, J., and Park, B. (2009). Variations in the Raman spectrum as a function of the number ofgraphene layers. J. Korean Phys. Soc. *55*, 1299–1303. https://doi.org/10.3938/jkps.55.1299.

37. Carr, D.W., Evoy, S., Sekaric, L., Craighead, H.G., and Parpia, J.M. (1999). Measurement of mechanical resonance and losses in nanometer scale silicon wires. Appl. Phys. Lett. *75*, 920–922. https://doi.org/10.1063/1.124554.

38. Kouh, T., Karabacak, D., Kim, D.H., and Ekinci, K.L. (2005). Diffraction effects in optical interferometric displacement detection in nanoelectromechanical systems. Appl. Phys. Lett. *86*, 013106. https://doi.org/10.1063/1.1843289.

39. Davidovikj, D., Poot, M., Cartamil-Bueno, S.J., van der Zant, H.S.J., and Steeneken, P.G. (2018). On-chip heaters for tension tuning of graphene nanodrums. Nano Lett. *18*, 2852–2858. https://doi.org/10.1021/acs.nanolett.7b05358.

40. Ye, F., Lee, J., and Feng, P.X.L. (2018). Electrothermally tunable graphene resonators operating at very high temperature up to 1200 K. Nano Lett. *18*, 1678–1685. https://doi.org/10.1021/acs.nanolett.7b04685.

41. Yoon, D., Son, Y.-W., and Cheong, H. (2011). Negative thermal expansion coefficient of graphene measured by Raman spectroscopy. Nano Lett. *11*, 3227–3231. https://doi.org/10.1021/nl201488g.

42. Mohiuddin, T.M.G., Lombardo, A., Nair, R.R., Bonetti, A., Savini, G., Jalil, R., Bonini, N., Basko, D.M., Galiotis, C., Marzari, N., et al. (2009). Uniaxial strain in graphene by Raman spectroscopy: *G* peak splitting, Grüneisen parameters, and sample orientation. Phys. Rev. B *79*, 205433. https://doi.org/10.1103/PhysRevB.79.205433.

43. Tsoukleri, G., Parthenios, J., Galiotis, C., and Papagelis, K. (2015). Embedded trilayer graphene flakes under tensile and compressive loading. 2D Mater. *2*, 024009. https://doi.org/10.1088/2053-1583/2/2/024009.

44. Cadelano, E., Palla, P.L., Giordano, S., and Colombo, L. (2009). Nonlinear elasticity of monolayer graphene. Phys. Rev. Lett. *102*, 235502. https://doi.org/10.1103/PhysRevLett.102.235502.

45. Goldsche, M., Sonntag, J., Khodkov, T., Verbiest, G.J., Reichardt, S., Neumann, C., Ouaj, T., von den Driesch, N., Buca, D., and Stampfer, C. (2018). Tailoring mechanically tunable strain fields in graphene. Nano Lett. *18*, 1707–1713. https://doi.org/10.1021/acs.nanolett.7b04774.

46. Wei, X., Fragneaud, B., Marianetti, C.A., and Kysar, J.W. (2009). Nonlinear elastic behavior of graphene: *Ab initio* calculations to continuum description. Phys. Rev. B *80*, 205407. https://doi.org/10.1103/PhysRevB.80.205407.

47. Wei, Y., and Yang, R. (2019). Nanomechanics of graphene. Natl. Sci. Rev. *6*, 324–348. https://doi.org/10.1093/nsr/nwy067.

48. Chaste, J., Eichler, A., Moser, J., Ceballos, G., Rurali, R., and Bachtold, A. (2012). A nanomechanical mass sensor with yoctogram resolution. Nat. Nanotechnol. *7*, 301–304. https://doi.org/10.1038/nnano.2012.42.

49. Dohn, S., Sandberg, R., Svendsen, W., and Boisen, A. (2005). Enhanced functionality of cantilever based mass sensors using higher modes. Appl. Phys. Lett. *86*, 233501. https://doi.org/10.1063/1.1948521.

50. Malvar, O., Ruz, J.J., Kosaka, P.M., Domínguez, C.M., Gil-Santos, E., Calleja, M., and Tamayo, J. (2016). Mass and stiffness spectrometry of nanoparticles and whole intact bacteria by multimode nanomechanical resonators. Nat. Commun. *7*, 13452. https://doi.org/10.1038/ncomms13452.

51. Hauer, B.D., Doolin, C., Beach, K.S.D., and Davis, J.P. (2013). A general procedure for thermomechanical calibration of nano/micro-mechanical resonators. Ann. Phys. (N. Y). *339*, 181–207. https://doi.org/10.1016/j.aop.2013.08.003.

52. Dean, C.R., Young, A.F., Meric, I., Lee, C., Wang, L., Sorgenfrei, S., Watanabe, K., Taniguchi, T., Kim, P., Shepard, K.L., and Hone, J. (2010). Boron nitride substrates for high-quality graphene electronics. Nat. Nanotechnol. *5*, 722–726. https://doi.org/10.1038/nnano.2010.172.

53. Ruz, J.J., Malvar, O., Gil-Santos, E., Calleja, M., and Tamayo, J. (2020). Effect of particle adsorption on the eigenfrequencies of nano-mechanical resonators. J. Appl. Phys. *128*, 104503. https://doi.org/10.1063/5.0021640.

54. Cleland, A.N., and Roukes, M.L. (2002). Noise processes in nanomechanical resonators. J. Appl. Phys. *92*, 2758–2769. https://doi.org/10.1063/1.1499745.

55. Djurić, Z.G., Jokić, I.M., Djukić, M.M., and Frantlović, M.P. (2010). Fluctuations of the adsorbed mass and the resonant frequency of vibrating MEMS/NEMS structures due to multilayer adsorption. Microelectron. Eng. *87*, 1181–1184. https://doi.org/10.1016/j.mee.2009.12.039.

56. Palasantzas, G. (2007). Adsorption-desorption noise influence on mass sensitivity and dynamic range of nanoresonators with rough surfaces. J. Appl. Phys. *101*, 076103. https://doi.org/10.1063/1.2714792.

57. Sansa, M., Sage, E., Bullard, E.C., Gély, M., Alava, T., Colinet, E., Naik, A.K., Villanueva, L.G., Duraffourg, L., Roukes, M.L., et al. (2016). Frequency fluctuations in silicon nanoresonators. Nat. Nanotechnol. *11*, 552–558. https://doi.org/10.1038/nnano.2016.19.

58. Yang, Y.T., Callegari, C., Feng, X.L., and Roukes, M.L. (2011). Surface adsorbate fluctuations and noise in nanoelectromechanical systems. Nano Lett. *11*, 1753–1759. https://doi.org/10.1021/nl2003158.

59. Yun, H., Kim, S., Kim, H., Lee, J., McAllister, K., Kim, J., Pyo, S., Sung Kim, J., Campbell, E.E.B., Hyoung Lee, W., and Wook Lee, S. (2015). Stencil nano lithography based on a nanoscale polymer shadow mask: towards organic nanoelectronics. Sci. Rep. *5*, 10220. https://doi.org/10.1038/srep10220.

60. Yao, S.K. (1979). Theoretical model of thin-film deposition profile with shadow effect. J. Appl. Phys. *50*, 3390–3395. https://doi.org/10.1063/1.326330.

61. Kim, Y.Y. (2017). An advanced characterization method for the elastic modulus of nanoscale thin-films using a high-frequency micromechanical resonator. Materials *10*, 806. https://doi.org/10.3390/ma10070806.

62. Nilsson, S.G., Borrisé, X., and Montelius, L. (2004). Size effect on Young's modulus of thin chromium cantilevers. Appl. Phys. Lett. *85*, 3555–3557. https://doi.org/10.1063/1.1807945.

63. Ekinci, K.L., Yang, Y.T., and Roukes, M.L. (2004). Ultimate limits to inertial mass sensing based upon nanoelectromechanical systems. J. Appl. Phys. *95*, 2682–2689. https://doi.org/10.1063/1.1642738.

64. Bolch, B.W. (1968). The teacher's corner: more on unbiased estimation of the standard deviation. Am. Stat. *22*, 27. https://doi.org/10.1080/00031305.1968.10480476.

65. Duncan, A.J. (1974). Other important sampling distributions. In In Quality control and industrial statistics (Irwin), p. 123.

66. Biswas, T.S., Xu, J., Miriyala, N., Doolin, C., Thundat, T., Davis, J.P., and Beach, K.S.D. (2015). Time-resolved mass sensing of a molecular adsorbate nonuniformly distributed along a nanomechnical string. Phys. Rev. Appl. *3*, 064002. https://doi.org/10.1103/PhysRevApplied.3.064002.

67. Bouchaala, A., Nayfeh, A.H., Jaber, N., and Younis, M.I. (2016). Mass and position determination in MEMS mass sensors: a theoretical and an experimental investigation. J. Micromech. Microeng. *26*, 105009. https://doi.org/10.1088/0960-1317/26/10/105009.

68. Chiu, H.Y., Hung, P., Postma, H.W.C., and Bockrath, M. (2008). Atomic-scale mass sensing using carbon nanotube resonators. Nano Lett. *8*, 4342–4346. https://doi.org/10.1021/nl802181c.

69. Jensen, K., Kim, K., and Zettl, A. (2008). An atomic-resolution nanomechanical mass sensor. Nat. Nanotechnol. *3*, 533–537. https://doi.org/10.1038/nnano.2008.200.

70. Jiang, C., Li, Q., Huang, J., Bi, S., Ji, R., and Guo, Q. (2020). Single-layer MoS_2 mechanical resonant piezo-sensors with high mass sensitivity. ACS Appl. Mater. Interfaces *12*,

41991–41998. https://doi.org/10.1021/acsami.0c11913.

71. Lassagne, B., Garcia-Sanchez, D., Aguasca, A., and Bachtold, A. (2008). Ultrasensitive mass sensing with a nanotube electromechanical resonator. Nano Lett. *8*, 3735–3738. https://doi.org/10.1021/nl801982v.

72. Sartori, A.F., Belardinelli, P., Dolleman, R.J., Steeneken, P.G., Ghatkesar, M.K., and Buijnsters, J.G. (2019). Inkjet-printed high-Q nanocrystalline diamond resonators. Small *15*, 1803774. https://doi.org/10.1002/smll.201803774.

73. Schwender, J. (2018). Mass Sensing with Graphene and Carbon Nanotube Mechanical Resonators (Universitat Politècnica de Catalunya). Doctoral thesis.

74. Yang, Y.T., Callegari, C., Feng, X.L., Ekinci, K.L., and Roukes, M.L. (2006). Zeptogram-scale nanomechanical mass sensing. Nano Lett. *6*, 583–586. https://doi.org/10.1021/nl052134m.

75. Barton, R.A., Ilic, B., van der Zande, A.M., Whitney, W.S., McEuen, P.L., Parpia, J.M., and Craighead, H.G. (2011). High, size-dependent quality factor in an array of graphene mechanical resonators. Nano Lett. *11*, 1232–1236. https://doi.org/10.1021/nl1042227.

76. Kumar, M., and Bhaskaran, H. (2015). Ultrasensitive room-temperature piezoresistive transduction in graphene-based nanoelectromechanical systems. Nano Lett. *15*, 2562–2567. https://doi.org/10.1021/acs.nanolett.5b00129.

77. Lee, H.-L., Yang, Y.-C., and Chang, W.-J. (2013). Mass detection using a graphene-based nanomechanical resonator. Jpn. J. Appl. Phys. *52*, 025101. https://doi.org/10.7567/JJAP.52.025101.

78. Lee, J., Wang, Z., He, K., Yang, R., Shan, J., and Feng, P.X.-L. (2018). Electrically tunable single- and few-layer MoS_2 nanoelectromechanical systems with broad dynamic range. Sci. Adv. *4*, eaao6653. https://doi.org/10.1126/sciadv.aao6653.

79. Parmar, M.M., Gangavarapu, P.R.Y., and Naik, A.K. (2015). Dynamic range tuning of graphene nanoresonators. Appl. Phys. Lett. *107*, 113108. https://doi.org/10.1063/1.4931118.

80. Alfaro, J.A., Bohländer, P., Dai, M., Filius, M., Howard, C.J., van Kooten, X.F., Ohayon, S., Pomorski, A., Schmid, S., Aksimentiev, A., et al. (2021). The emerging landscape of single-molecule protein sequencing technologies. Nat. Methods *18*, 604–617. https://doi.org/10.1038/s41592-021-01143-1.

81. Gupta, N., Tanner, S., Jaitly, N., Adkins, J.N., Lipton, M., Edwards, R., Romine, M., Osterman, A., Bafna, V., Smith, R.D., and Pevzner, P.A. (2007). Whole proteome analysis of post-translational modifications: applications of mass-spectrometry for proteogenomic annotation. Genome Res. *17*, 1362–1377. https://doi.org/10.1101/gr.6427907.

82. Jiao, L., Fan, B., Xian, X., Wu, Z., Zhang, J., and Liu, Z. (2008). Creation of nanostructures with poly(methyl methacrylate)-mediated nanotransfer printing. J. Am. Chem. Soc. *130*, 12612–12613. https://doi.org/10.1021/ja805070b.

83. Kim, Y., Yun, H., Nam, S.-G., Son, M., Lee, D.S., Kim, D.C., Seo, S., Choi, H.C., Lee, H.-J., Lee, S.W., and Kim, J.S. (2013). Breakdown of the interlayer coherence in twisted bilayer graphene. Phys. Rev. Lett. *110*, 096602. https://doi.org/10.1103/PhysRevLett.110.096602.

STAR★METHODS

KEY RESOURCES TABLE

REAGENT or RESOURCE	SOURCE	IDENTIFIER
Chemicals, peptides, and recombinant proteins		
Graphite flake	NGS Trading & Consulting GmbH	https://www.graphit.de/
Potassium hydroxide	Sigma Aldrich	CAS: 1310-58-3
950 PMMA C4	MicroChem Corporation	https://kayakuam.com/
Methyl isobutyl ketone	MicroChem Corporation	CAS Number: 108-10-1
Software and algorithm		
Origin	OriginLab Corporation	https://www.originlab.com
Other		
Optical microscope	OLYMPUS Corporation	https://www.olympus-lifescience.com
Electron microscope	Tescan	Tescan MIRA2
Spectrometer	HORIBA Jobin Yvon	Jobin-Yvon Triax 320
Atomic force microscope	Park Systems	NX10
Raith ELPHY Quantum	Raith	https://www.raith.com
Critical point dryer	tousimis research corporation	Autosamdri-815

RESOURCE AVAILABILITY

Lead contact

Further information and other requests should be directed to and will be fulfilled by the lead contact, Sang Wook Lee (leesw@ewha.ac.kr).

Materials availability

This work did not generate new unique reagents.

Data and code availability

- All data reported in this paper will be shared by the lead contact upon request.
- This paper does not report original code.
- Any additional information required to reanalyze the data reported in this paper is available from the lead contact upon request.

METHOD DETAILS

Fabrication of graphene resonators

Graphene was prepared by a mechanical exfoliation method using Scotch tape. The 2D peak shape and the 2D to G peak ratio of Raman spectroscopy was used to determine the number of graphene layers.[34–36] Graphene with three atomic layers was selected and patterned into a ribbon shape by electron beam lithography and reactive ion etching processes, and then 50 nm of gold was deposited on both ends of the graphene ribbons using electron beam lithography and electron beam evaporation methods. Poly(methyl methacrylate) (PMMA) 950K C4 was spin-coated on the substrate at 4500 rpm followed by baking at 180 °C for 5 minutes. The PMMA film with graphene ribbons was separated from SiO_2/Si substrate in 4M KOH solution. The graphene surface was rinsed with deionized water to remove KOH and dried at room temperature in N_2 atmosphere. The graphene ribbon was transferred onto a pre-fabricated electrode structure by using a micro-positioner.[82,83] To fix the graphene ribbon tightly on the metal electrode, cross-linked PMMA was formed at the both ends of the suspended graphene ribbon by high-dose electron beam lithography.

Finally, the critical point drying process was carried out after removal of PMMA using acetone and isopropanol alcohol to prevent the collapse of the suspended structure. The process flow used to fabricate the graphene mass sensor device is illustrated in Figure S1.

Joule heating-induced ultra-high temperature annealing

The voltage sweep was performed carefully to prevent the suspended graphene from breaking due to excessive heat generation. We set a voltage whose current does not exceed 100 μA as the maximum voltage, performed a voltage sweep, and repeated the voltage sweep while gradually increasing the maximum voltage setting, as shown in Figure S2. If the *IV* curve exhibited a highly non-linear shape, the voltage sweep was repeated with the same maximum voltage set until the *IV* curve became linear. After visible light emitted from graphene and reduced differential conductance were observed, the device was sufficiently annealed by maintaining the maximum voltage constant and repeating the voltage sweep.

Raman spectroscopy measurement

The Raman spectra were measured using the 514.5 nm line of an Ar ion laser or the 441.6-nm line of a He–Cd laser with a power of 500-μW, focused with a 50× objective lens (NA 0.42). The scattered light was collimated by the same objective and focused onto the entrance slit of a Jobin-Yvon Triax 320 spectrometer (1,200 grooves/mm), and a CCD array was used to record the spectra.

Dynamic flexural measurement

The resonance frequency of the graphene resonator was measured using optical interferometry.[21,37,38] Several frequency sweeps (3–7 sweeps) were performed at every experimental stage (before annealing, after annealing, and after the 1st, 2nd, and 3rd mass loading), as shown in Figure S3 and Table S1, with an integration time of 0.1sat low vacuum (~10^{-3} Torr) and room temperature conditions. The graphene resonators were actuated to vibrate at their resonance frequency by electrostatic forces, that act between the graphene and the Si substrate, generated by an AC gate bias. When the AC frequency applied between the suspended graphene and the gate electrode matches the mechanical resonance frequency of the graphene membrane, the graphene mass sensor exhibits resonance behavior. The power intensity of 633 nm He-Ne laser was attenuated to be around 80 μW to minimize thermally induced stress or structural deformation of the suspended graphene ribbon structure. Although the intensity of reflected laser from the graphene surface is very small due to its high transparency, the position dependent absorption of the graphene in the standing light wave that is formed near the substrate also contributes to modulation of the reflected light, such that the laser interferometry detection technique has enough sensitivity for clearly recognizing motion.

Preparation of PMMA stencil mask

PMMA C4 was spin-coated on a SiO_2/Si substrate at 4500 rpm followed by baking at 180 °C for 5 minutes. This was repeated twice to obtain a mask with a thickness of about 550 nm. Then, a line shaped pattern with a dimension of 0.5 μm × 50 μm was defined on the PMMA membrane by using electron beam lithography technique. The line patterned PMMA membrane was lifted by chemically removing the SiO_2 layer and transferred to supporting posts of the graphene resonator. The supporting posts with a 0.3 mm thickness were used to maintain around 300 μm of gap between the suspended graphene ribbon and the PMMA stencil mask.